
LEARNED SINGLE-PIXEL FLUORESCENCE MICROSCOPY

Serban C. Tudosie^{1,*} Valerio Gandolfi² Shivaprasad Varakkoth²

Andrea Farina³ Cosimo D'Andrea^{2,3,4} Simon Arridge¹

ABSTRACT

Single-pixel imaging has emerged as a key technique in fluorescence microscopy, where fast acquisition and reconstruction are crucial. In this context, images are reconstructed from linearly compressed measurements. In practice, total variation minimisation is still used to reconstruct the image from noisy measurements of the inner product between orthogonal sampling pattern vectors and the original image data. However, data can be leveraged to learn the measurement vectors and the reconstruction process, thereby enhancing compression, reconstruction quality, and speed. We train an autoencoder through self-supervision to learn an encoder (or measurement matrix) and a decoder. We then test it on physically acquired multispectral and intensity data. During acquisition, the learned encoder becomes part of the physical device. Our approach can enhance single-pixel imaging in fluorescence microscopy by reducing reconstruction time by two orders of magnitude, achieving superior image quality, and enabling multispectral reconstructions. Ultimately, learned single-pixel fluorescence microscopy could advance diagnosis and biological research, providing multispectral imaging at a fraction of the cost.

Keywords Single-Pixel Imaging, Machine Learning, Inverse Problems, Fluorescence Microscopy

1 Introduction

Fluorescence microscopy is widely used for cell and tissue imaging and is a fundamental tool in biomedical research [1]. To image samples in this context, charge-coupled device (CCD) and complementary metal-oxide-semiconductor (CMOS) cameras are a common choice. Acquiring multispectral information is often desirable but requires costly, slow, and inefficient solutions with tunable spectral filters or point acquisition with a raster scan over the sample [2, 3]. The single-pixel camera (SPC) [4] is a new imaging paradigm that can make multispectral acquisitions faster and more efficient, and has been recently applied to multispectral fluorescence microscopy [5]. It relies on the principles of compressive sensing (CS) [6], where compression takes place during observation, thus acquiring a compressed representation of the imaged scene from which the image can be reconstructed. An SPC system uses an underdetermined linear measurement matrix and a reconstruction algorithm. The measurement matrix and the reconstruction algorithm can be constructed using the principles of CS theory or learned from data [7] through self-supervision with an autoencoder. These approaches require learning a physics-constrained encoder (binary, linear, and underdetermined) and a decoder that jointly reconstructs and denoises. For conventional SPC systems, learned approaches have recently shown advantages in terms of reconstruction quality and speed [8, 7, 9]. A crucial aspect of SPC, in particular, applied to fluorescence microscopy, is reconstructing images as fast as possible to enable real-time imaging for the medical field.

To our knowledge, there are no studies about the benefit that learned approaches could provide to SPC systems for fluorescence microscopy. In addition, it is unclear how essential the training data distribution is for learned single-pixel

¹ Department of Computer Science, University College London, 66-72 Gower St, WC1E6EA London, UK

² Dipartimento di Fisica, Politecnico di Milano, Piazza L. da Vinci 32, 20133 Milano, Italy

³ Consiglio Nazionale delle Ricerche, Piazza L. da Vinci 32, 20133 Milano, Italy

⁴ Center for Nano Science and Technology, Istituto Italiano di Tecnologia, Via Raffaele Rubattino, 81, 20134 Milano, Italy

* sc.tudosie.23@ucl.ac.uk

imaging (SPI). Thus, it is essential to determine whether a model for single-pixel imaging trained on natural images can be applied effectively in other applications where data availability is limited.

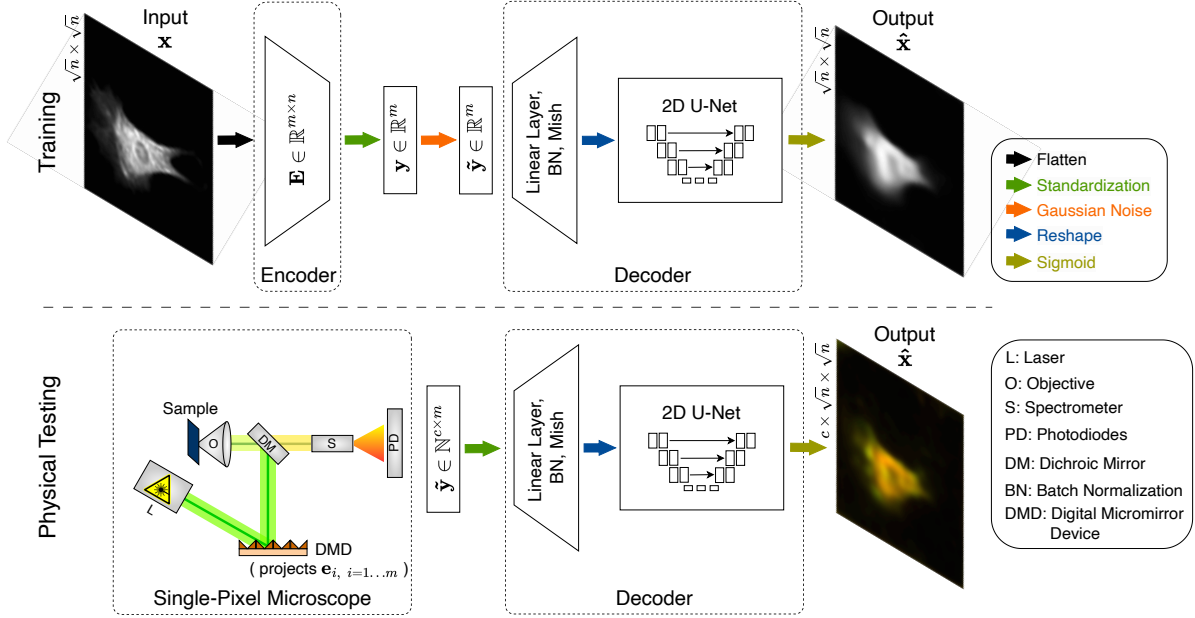


Figure 1: Network architecture. We show the training phase (upper part) and the multispectral physical testing (lower part). At the end of the training phase, \mathbf{E} becomes binary. At test time, the decoder can be used over multiple spectral channels, using the batch dimension to create an output image with c channels; or, the spectral channels can be integrated so that the decoder can be tested on single-channel measurements. The microscope box reports the setup of the single-pixel multispectral fluorescence microscope.

These questions motivate the current study, which aims to develop an autoencoder that is easily trainable for SPC microscopy setups, works in the multispectral setting, and can achieve real-time reconstructions. We showcase how it behaves at different noise levels, compression percentages, and training datasets. We then compare it with standard CS approaches. We additionally use the measurement matrix learned by the model’s encoder for experimental measurements with an SPC-based multispectral fluorescence microscope setup and then reconstruct with its learned decoder, comparing the results to standard CS approaches.

2 Methods

2.1 Single-Pixel Camera

The SPC [4] is an imaging technique that exploits structured light illumination (or detection) and a single-pixel photodetector [10]. The SPC fluorescence microscope used in our physical measurements generates structured light illumination through a digital micromirror device (DMD). A laser illuminates the DMD, producing a series of spatial light patterns by turning individual mirrors on or off. Each pattern creates a single measurement with the photodetector – a dot product between the scene and the pattern. The multispectral acquisition is obtained by coupling the SPC with a spectrometer and an array of single-pixel photodetectors, such that each photodetector captures a different spectral band. In the multispectral setting, the same pattern is used for each band.

The forward procedure is linear and can be expressed as $\mathbf{y} = \mathbf{A}\mathbf{x}$, where $\mathbf{y} \in \mathbb{R}^{m \times 1}$ is the measurement vector, $\mathbf{x} \in \mathbb{R}^{n \times 1}$ is the image, $\mathbf{A} \in \{0, 1\}^{m \times n}$ is the measurement matrix (we will refer to this matrix as "patterns" or "encoder" as they perform the same function); $m, n \in \mathbb{N}$. Practically, each row in \mathbf{A} gets reshaped into a $\sqrt{n} \times \sqrt{n}$ pattern, which the DMD can expose. \mathbf{A} must be binary, i.e. $\in \{0, 1\}^{m \times n}$ for physical requirements of DMDs. The goal is to retrieve \mathbf{x} . In a noiseless setting, if \mathbf{A} is invertible, retrieving \mathbf{x} is trivial, $\mathbf{x} = \mathbf{A}^{-1}\mathbf{y}$. However, in physical

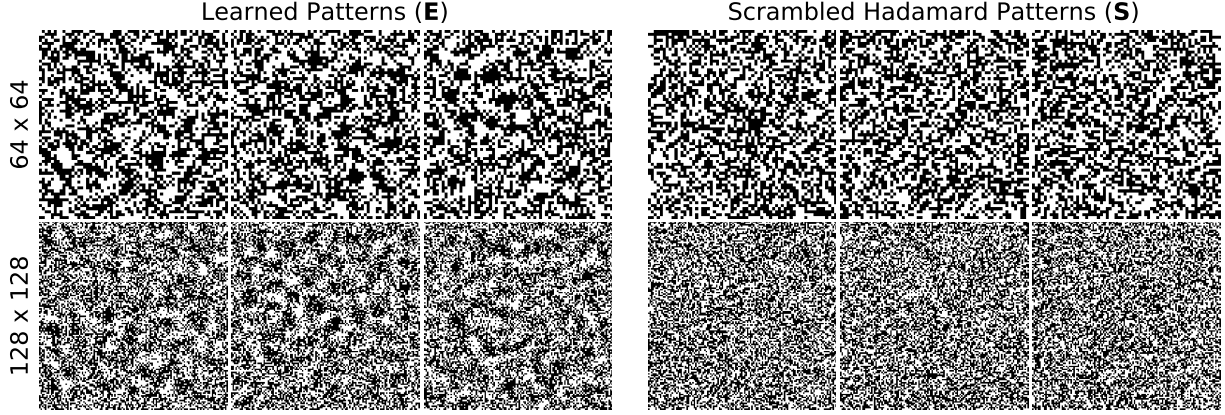


Figure 2: Patterns from the learned encoder (left) and \mathbf{S} patterns (right) for 64×64 (top) and 128×128 (bottom). We show three random rows from the measurement matrices reshaped in their 2D representation. These 2D patterns correspond to the structured light emitted on the sample.

SPC systems, noise is always present due to the discrete nature of photons and the fluctuations in circuits. This results in a Poisson-Gaussian noise model

$$\tilde{\mathbf{y}} = \gamma \mathbf{z} + \epsilon, \text{ where } \mathbf{z} \sim \mathcal{P}\left(\frac{\mathbf{A}\mathbf{x}}{\gamma}\right) \text{ and } \epsilon \sim \mathcal{N}(0, \sigma^2 \mathbf{I}). \quad (1)$$

Additionally, most applications aim to have a fast acquisition time, i.e. reducing m as much as possible, which makes the problem underdetermined.

CS plays a key role in the SPC setting. CS states that retrieving a signal by randomly sampling it, even at a sub-Nyquist rate, is possible if the signal is sparse in some domain, e.g. Fourier. Thus, we can retrieve \mathbf{x} at $m \ll n$ measurements, but \mathbf{A} must be incoherent to the basis in which the signal is sparse and must respect the restricted isometry property [11]. Scrambled Hadamard (\mathbf{S}) patterns [12] are a common choice for \mathbf{A} since they are orthogonal, pseudo-random, and $\mathbf{S} \in \{-1, 1\}^{m \times n}$, i.e. more adequate for CS. To directly adapt them to the optical setup, we will consider \mathbf{S} patterns where -1 entries are mapped to 0, and we will refer to these patterns again as \mathbf{S} . This choice comes at the loss of orthogonality. Thus, in practice, in a noisy, compressed setting ($m < n$), a common procedure is to approximately retrieve \mathbf{x} by total variation (TV) regularisation, solving an ROF [13] model with \mathbf{S} measurement matrix:

$$\min_{\mathbf{x}} \frac{\mu}{2} \|\mathbf{S}\mathbf{x} - \mathbf{y}\|_2^2 + \text{TV}(\mathbf{x}). \quad (2)$$

TVAL3 [14] is an efficient algorithm to approximate \mathbf{x} for SPC, often used in fluorescence microscopy [5]. Alternatively, it is possible to learn from data an underdetermined \mathbf{A} together with a decoding function D_θ parametrised by θ , through a self-supervised autoencoder [7]. Then, physically measure with a learned \mathbf{A} and reconstruct with D_θ at test time. We will refer to the learned \mathbf{A} matrices as \mathbf{E} .

2.2 Our Approach

We use an autoencoder to jointly learn a binary linear underdetermined \mathbf{E} and a reconstruction network D_θ (Fig. 1). We take inspiration from [7] and [8], where an $\mathbf{E} \in \{-1, 1\}^{m \times n}$ is learned from data, while the decoder learns to denoise and reconstruct the image from a noisy latent space (simulated measurements). However, in contrast to previous works, we modify the losses and the reconstruction network. In more detail, we change the binarisation penalty term (\mathcal{L}_B) so that $\mathbf{E} \in \{0, 1\}^{m \times n}$ at the end of the training, instead of $\mathbf{E} \in \{-1, 1\}^{m \times n}$. The latter would require $2 \times m$ measurements (first the positive patterns and then negative ones) since an optical setup with one DMD can encode only 0 (dark pixel) and 1 (bright pixel). We thus use the following non-convex binarisation penalty on \mathbf{E} :

$$\mathcal{L}_B(\mathbf{E}) = \frac{\lambda}{mn} \sum_{i=1}^m \sum_{j=1}^n (e_{ij} - 1)^2 e_{ij}^2. \quad (3)$$

The parameter λ is dynamic. At each network update, starting from 0, we increase λ by $\frac{1}{TS}$, where TS is the total number of training steps. When $\mathcal{L}_B(\mathbf{E})$ stops improving, we stop updating \mathbf{E} and continue training to further adapt

D_θ to the completely binarised \mathbf{E} . We initialise \mathbf{E} from a beta distribution $e_{ij} \sim \mathcal{B}(\alpha, \beta)$ with $\alpha = \beta = 0.7$, which empirically provides faster training. Then, we use a combination of L1 loss ($\mathcal{L}_1(\mathbf{x}, \hat{\mathbf{x}}) := \|\mathbf{x} - \hat{\mathbf{x}}\|_1$) and SSIM loss ($\mathcal{L}_{\text{SSIM}}(\mathbf{x}, \hat{\mathbf{x}}) := 1 - \text{SSIM}(\mathbf{x}, \hat{\mathbf{x}})$) for our data fidelity term since their combination has been proven ideal for image restoration tasks [15]. In summary, we solve the following problem:

$$\min_{\mathbf{E}, \theta} \frac{1}{|\mathcal{D}|} \sum_{i=1}^{|\mathcal{D}|} \left[\overbrace{w_1 \mathcal{L}_1(\mathbf{x}^{(i)}, \hat{\mathbf{x}}^{(i)})}^{\text{Intensity}} + \overbrace{w_2 \mathcal{L}_{\text{SSIM}}(\mathbf{x}^{(i)}, \hat{\mathbf{x}}^{(i)})}^{\text{Structure}} \right] + \overbrace{w_3 \mathcal{L}_B(\mathbf{E})}^{\text{Binarisation}}, \quad (4)$$

where $\hat{\mathbf{x}}$ is the reconstruction $D_\theta(\mathbf{E}\mathbf{x} + \epsilon)$, $w_1, w_2, w_3 \in \mathbb{R}$ are weights that we set to 0.2, 0.8, and 16, respectively, and $|\mathcal{D}|$ is the cardinality of the dataset. We only focus on additive Gaussian noise for simplicity. We standardise the measurements $\mathbf{y} = \mathbf{E}\mathbf{x}$ (instance normalization [16] without learnable parameters). Standardisation is crucial for adapting the decoder to real measurements, as different acquisitions might have different means that depend on the power of the laser, exposure time, and the sample itself. To the standardised measurements, we add Gaussian noise to learn a decoder that also performs denoising.

For D_θ , we employ a linear layer followed by a 2D U-Net [17]. We use Mish [18] to introduce non-linearities and Adam [19] to optimise. Note that the network has non-linearities only in D_θ as the forward process is purely linear to match the physics and design of the single-pixel camera microscope. Fig. 1 shows the network diagram at training and physical testing times. In this paper, we refer to our approach as learned encoder-decoder (LED).

2.3 Datasets

We employ a reduced version of CytoImageNet [20], a single-channel microscopy dataset with cellular images. In particular, we are interested in image sizes of 64×64 and 128×128 . In structured illumination microscopy, larger image sizes are unfeasible, since higher pattern resolutions reach the diffraction limit for projected patterns. For training, validation, and testing, we randomly select, respectively, 100,000, 10,000, and 1,000 images, each at a size of 128×128 . We call this dataset Cyto128. Then, we downscale this dataset to 64×64 to create Cyto64. We use a small test set since TV-based approaches require orders of magnitude more time to retrieve the image.

To demonstrate the generalisation capability of the network, we also use 100,000 images from the STL10 dataset [21] to train a LED model (STL-LED). This dataset contains natural images, e.g. horses and cars. We then test it on cellular data.

To show the applicability of LED on real-world measurements for fluorescence microscopy, we experimentally acquire a test set on a biological sample. We use bovine pulmonary artery endothelial cells (FluoCells™ Prepared Slide #1, Invitrogen™). From this slide, we collect 3 field of views (FOVs) of $150 \mu\text{m} \times 150 \mu\text{m}$. The cells are stained with multiple fluorescent dyes and will show different emission spectra in separate parts of the cell under multispectral imaging. Particularly, cell membranes should emit at 512 nm, while mitochondria at 599 nm. Additionally, we couple the microscope with an extra output to a CMOS camera to provide a ground truth intensity image. Thus, each entry in the test set is made of a CMOS image (spatial ground truth), compressed multispectral single-pixel measurements with learned \mathbf{E} patterns, compressed multispectral single-pixel measurements with \mathbf{S} patterns, and uncompressed multispectral single-pixel measurements with \mathbf{S} patterns (to reconstruct the spectral ground truth image).

3 Experiments

3.1 Noise-Compression Model Behaviour

We train LED models on Cyto64 and Cyto128 training sets at 6 different training noise levels (standard deviation σ of additive Gaussian noise), and then, at test time, we add noise with $\sigma = 0.25$ (Fig. 3 left). We also train at 5 different compression percentages $CP := 100(1 - m/n)$ and a fixed noise level (Fig. 3 right). We test the trained models on Cyto64 and Cyto128 test sets. We observe that the models depend on the training noise level in a non-monotonic fashion. In other words, a model trained at $\sigma = 0.5$ and tested at $\sigma = 0.25$ will perform worse than a model trained at $\sigma = 0.25$ and tested at $\sigma = 0.25$. This suggests that for excessively large training σ , the models stop benefiting from the addition of noise, and it may be beneficial to train with different noise σ s to increase robustness. Compression plays an important role on test structural similarity index measure (SSIM) and peak signal-to-noise ratio (PSNR). More compression results in faster acquisitions and reduced photobleaching, albeit at the expense of lower-quality reconstructions. Between acquiring at $CP = 95$ to $CP = 75$ the 64×64 models have a 0.1 increase in SSIM. We show a reconstruction with LED models from the Cyto test sets in Fig. 4. LED models maintain lower frequencies when constrained to high compression (Fig. 4 204 patterns) and gradually include higher frequencies for lower compression

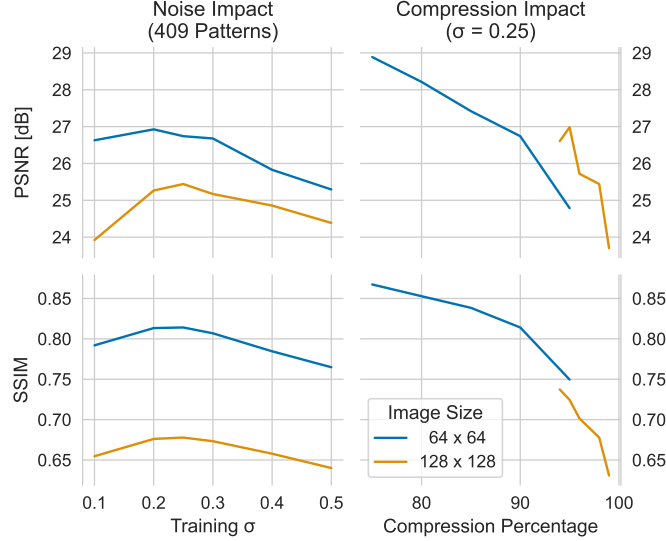


Figure 3: Noise (left) and compression (right) impact on LED’s performance on Cyto64 and Cyto128 test sets. We show PSNR and SSIM to quantify performance. To evaluate the noise impact on the model, we fix the number of patterns at 409; similarly, to evaluate the compression, we fix the noise at a standard deviation $\sigma = 0.25$.

constraints (Fig. 4 1024 patterns); similarly to how an inverse Fourier transform from the k -highest coefficients would act at different thresholds k .

3.2 Performance on Simulated Measurements

Considered Methods.

We now compare different methods for acquiring the compressed measurements and reconstructing the image. We experiment with simulated measurements from images from Cyto64 and Cyto128 test sets. In particular, we consider the following methods: SH-TVAL3, LE-TVAL3, SH-LD, DCAN, STL-LED, and LED. SH-TVAL3 consists of measuring with \mathbf{S} patterns and reconstructing with TVAL3. LE-TVAL3, instead, first learns the patterns with a LED model, then measures with the learned \mathbf{E} but reconstructs with TVAL3. SH-LD learns the decoder by training a LED model with a frozen measurement matrix \mathbf{S} patterns. DCAN is the model from [7] trained with our loss function, weight initialisation, and latent space standardisation. STL-LED is a LED model trained on natural images from the STL10 dataset instead of microscopy images; all the other LED-based methods and DCAN are trained on Cyto64 and Cyto128 datasets. We add noise with $\sigma = 0.25$ for all methods and fix the compression to 409 patterns ($CP = 90$) for 64×64 images and 614 patterns ($CP = 96$) for 128×128 images. TVAL3-based reconstruction requires setting 2 parameters of the algorithm, μ and β ; which we set in the following way: $\mu = 2^9, \beta = 2^4$ for SH-TVAL3 and $\mu = 2^7, \beta = 2^4$ for LE-TVAL3.

Methods Comparison. Table 1 shows a comparison between the considered methods in terms of SSIM, PSNR, and time required to reconstruct. We can observe that learning either the measurement matrix or the decoder benefits the

Image Size	Metric	SH-TVAL3	LE-TVAL3	SH-LD	DCAN	STL-LED	LED
64×64	SSIM	0.39 ± 0.10	0.51 ± 0.10	0.60 ± 0.13	0.71 ± 0.10	0.74 ± 0.13	0.82 ± 0.09
	PSNR [dB]	15.59 ± 3.87	18.3 ± 3.21	21.38 ± 3.20	23.37 ± 2.89	22.19 ± 3.70	26.61 ± 3.12
	Time [ms]	418 ± 310	662 ± 467	11 ± 8	4 ± 3	11 ± 5	14 ± 7
128×128	SSIM	0.23 ± 0.08	0.44 ± 0.12	0.50 ± 0.14	0.62 ± 0.13	0.63 ± 0.15	0.71 ± 0.13
	PSNR [dB]	12.53 ± 2.87	17.13 ± 3.59	20.22 ± 3.16	23.6 ± 3.30	21.46 ± 3.37	25.67 ± 3.74
	Time [ms]	469 ± 524	636 ± 1095	23 ± 13	9 ± 4	22 ± 9	26 ± 14

Table 1: Comparison of methods on the Cyto64 and Cyto128 test sets, reporting mean \pm standard deviation of SSIM, PSNR, and reconstruction time. In this case, we use 409 patterns for the 64×64 comparisons and 614 for the 128×128 ones with a fixed $\sigma = 0.25$.

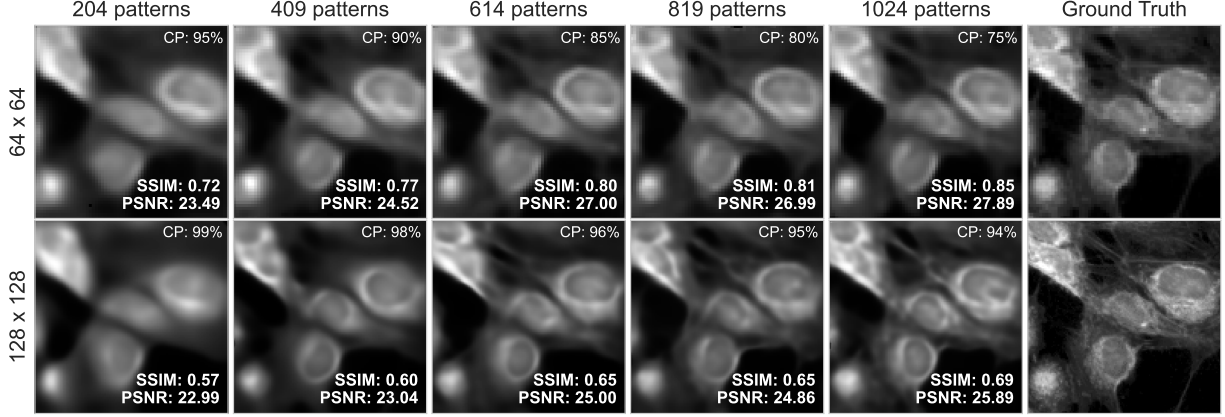


Figure 4: Reconstructions on an image from the test sets Cyto64 (first row) and Cyto128 (second row) with LED models trained with different compression levels. For each model, we report SSIM, PSNR, and the compression percentage CP. The last column shows the corresponding ground truth.

reconstruction quality. Additionally, using a learned decoder instead of solving the inverse problem for each image takes significantly less reconstruction time. The smallest decoder (DCAN) requires, on average, 4 ms to reconstruct 64×64 images, while the TVAL3 reconstructions can take 100 times longer. LED improves in both SSIM and PSNR with respect to the DCAN approach. Lastly, we show that LED can generalise by training it on the STL10 dataset (STL-LED) and testing it on Cyto64 and Cyto128 (Table 1). TVAL3 reconstruction quality depends extensively on the choice of the internal parameters μ and β , making it difficult to select the optimal parameters over a large and diverse set of images. In contrast, with learned approaches, the hyperparameters can be chosen using the validation set, making the reconstruction quality at test time more consistent and parameter-free. We compute the reconstructions for the comparisons on the test sets on an Apple Silicon M3 CPU.

Patterns Comparison. In Fig. 2 we show the learned patterns and the \mathbf{S} patterns. Learned patterns exhibit more structure and lower frequencies. During training, we leave the patterns unconstrained (besides the binarisation term in the loss). However, after training, the learned patterns reach a fill factor: $\frac{1}{mn} \sum_{i=1}^m \sum_{j=1}^n e_{ij}$, of 0.5 which corresponds to the fill factor of \mathbf{S} patterns. In addition, the learned ones exhibit quasi-orthogonal properties, similarly to \mathbf{S} patterns. Thus, most of the singular values of \mathbf{E} are constant (making each pattern contribution to the measurements maximally informative).

4 Physical Testing

4.1 Intensity Reconstructions

First, we work with fluorescence intensity measurements (single channel measurements without spectral information), as in the model. We obtain the measurements by summing the data from the multispectral SPC microscope along the axis corresponding to the spectrum. We find that LED models can significantly improve the reconstruction quality and speed on a physical single-pixel microscope (Fig. 5). We compare four methods: SH-TVAL3, LE-TVAL3, SH-LD, and LED for three FOVs. We demonstrate that prior learning of the patterns can aid the TVAL3 reconstruction, improving cellular structure (Fig. 5 LE-TVAL3), e.g. in FOV 1 and FOV 2, the cell membranes maintain a closer structure to the GT image. Similarly, learning the decoder with \mathbf{S} encoding (SH-LD) reduces background noise, improving all metrics. Finally, LED benefits from both effects. Time is significantly reduced when using the learned decoder because instead of solving a minimisation problem for each acquisition, it just applies the learned mapping D_θ . We remark that reducing reconstruction time is crucial in translating current single-pixel microscopy into real-time imaging.

4.2 Multispectral Reconstructions

We additionally find that LED models can be applied to multispectral imaging (Fig. 6). In this context, the measurements are multispectral, i.e. each pattern produces c measurements as shown in Fig. 1, at c different wavelengths. We thus reconstruct multispectral images by applying the four previous methods to each channel separately (Fig. 6). However, models that reconstruct with the learned decoder standardise the latent space. To account for different channel intensities

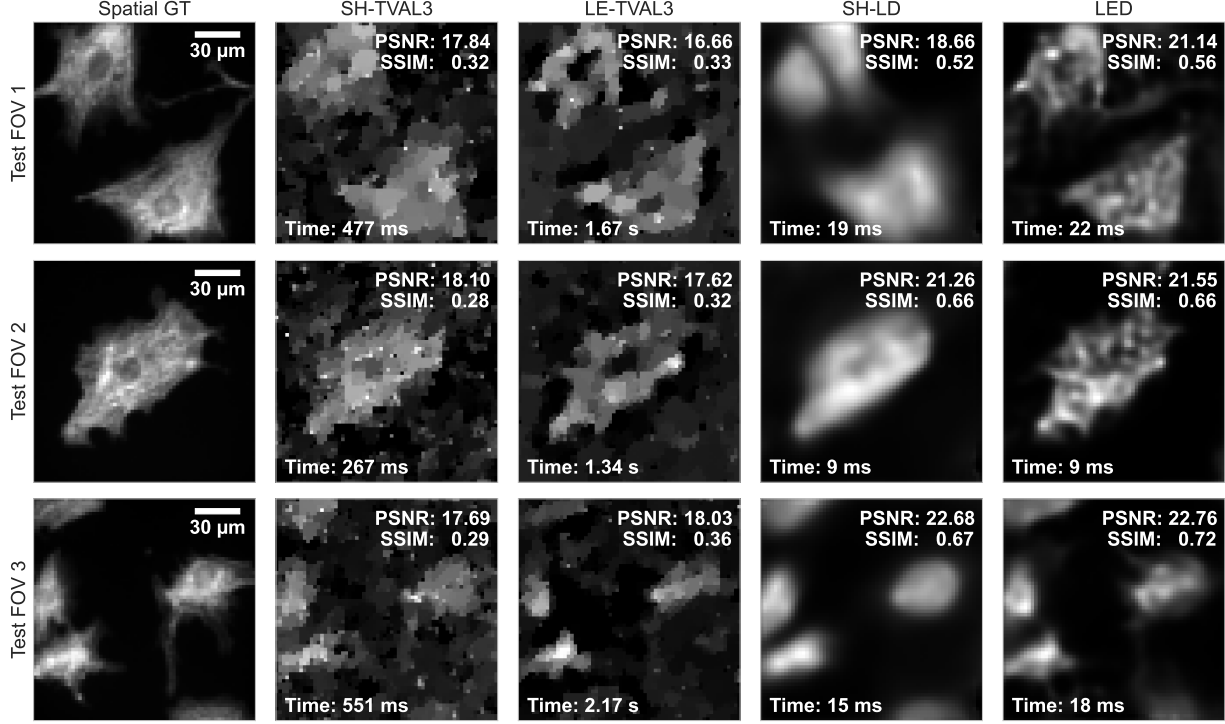


Figure 5: Comparison between single-pixel intensity imaging approaches on a physical microscope at 90% compression. Each row shows a different test sample. The first column represents the spatial intensity GT. The following columns show the different approaches. For each reconstruction, we report PSNR, SSIM (top right), and reconstruction time (bottom left).

(i.e. the spectral shape), we save the normalised channel means of the measurements before applying standardisation and then, after the reconstruction, we multiply each of the channels by the saved mean. Since the images from the CMOS camera are not multispectral, we acquire the entire basis of \mathbf{S} patterns and use the inverse \mathbf{S} matrix to retrieve an image for each channel of the single-pixel measurements. We consider this inversion the spectral GT. Without further denoising, this GT will look corrupted by Poisson-Gaussian noise. However, in this case, we focus on showing the capability of reconstructing multispectral images at a reduced computational time. Fig. 6 shows the enormous reduction in reconstruction time for 64×64 images with 16 spectral channels, while maintaining similar image quality. The cells are correctly reproduced, with the yellow-green colour highlighting the membrane and the orange colour in the inner part highlighting the mitochondria.

5 Conclusion

A crucial aspect of single-pixel camera fluorescence microscopy systems is to make image reconstruction fast and reliable. We demonstrate that it is possible to apply a learning paradigm to such systems, thereby improving upon classical CS approaches in terms of reconstruction speed and image quality. We showcase the comparison on a physical setup for intensity and multispectral reconstructions, thus demonstrating a real-world application of our model. Additionally, we show that the model exhibits particular generalisation capabilities, as by training on natural images, we can still reconstruct cellular images with a similar performance to the model trained on cellular images. This opens new avenues in learned SPI applied to scenarios where data is scarce, e.g. endoscopy.

The current limitation of learned SPI is the unmatched noise modelling with respect to the real-world case. This can be seen directly from the performance of the models on the Cyto64 test set (0.82 SSIM) compared to the reconstructions from the real-world measurements (0.65 SSIM). Here, we have only considered the additive Gaussian noise case; however, a more realistic case in SPCs is Poisson-Gaussian noise 1, which should be considered in future works. Additionally, SPC fluorescence microscopes can be coupled with an additional device (a time-correlated single photon counter [23]) to produce an extra temporal dimension in the measurement for each pattern – sampling fluorescence decay over time. The lifetime of the decay can help investigate metabolic processes [24, 25]. We currently limit the

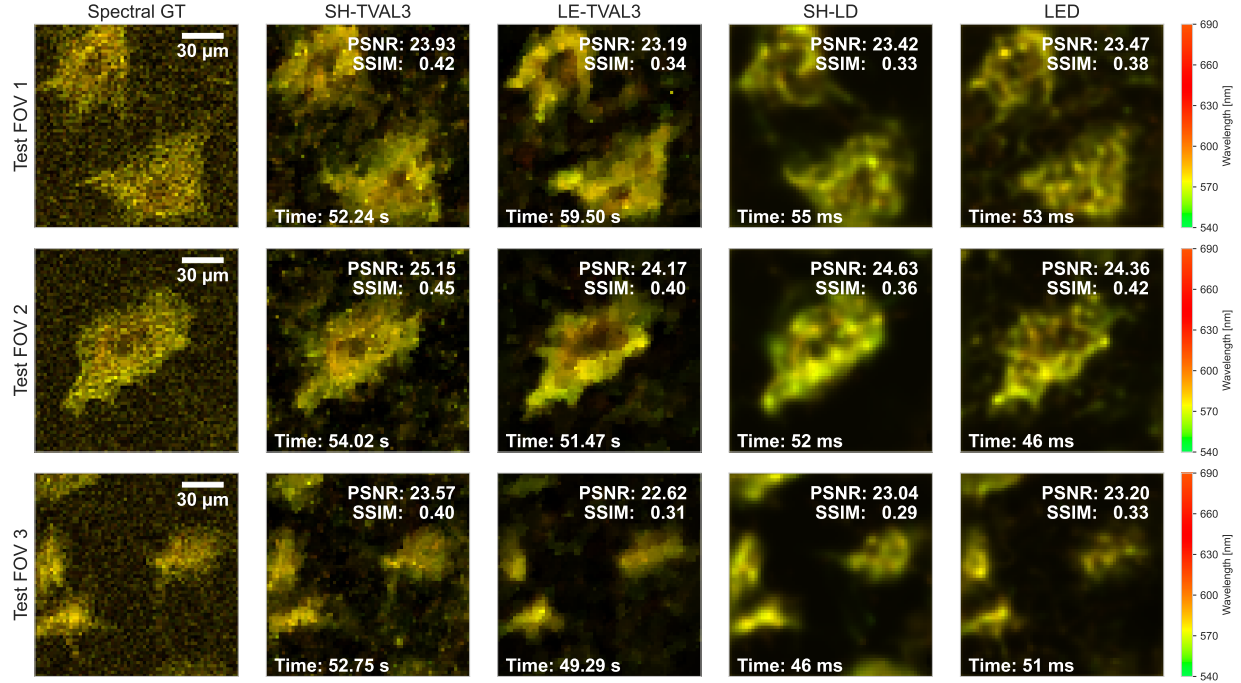


Figure 6: Comparison between single-pixel multispectral imaging approaches on the physical microscope. Each spectral channel undergoes 90% compression. Each row shows a different test sample. The first column represents the GT. The following columns show the different approaches. The colour bar shows the detector wavelength range. For convenience of plotting, the 16-channel spectral images are transformed to sRGB using the CIE standard colour-matching functions [22]. For each reconstruction, we report the PSNR over the entire cube, the mean SSIM of the 16 channels (top right), and reconstruction time (bottom left).

application of learned SPI to multispectral and intensity measurements. Lastly, an apparent limitation could appear to be the reduced image size. However, SPC microscopy systems similar to the one shown in Fig. 1 are usually coupled with a high-resolution CMOS camera. The intensity CMOS image and the multispectral single-pixel reconstruction can be combined through data fusion [26, 5], providing a high-resolution multispectral image, without the need for a multispectral or hyperspectral CMOS sensor, and the potential to work in the infrared range and beyond.

Future work could enhance the robustness of learned SPI in microscopy by attempting to denoise measurements affected by Poisson-Gaussian noise during training. The validity and application of learned SPI approaches in the lifetime imaging setting are yet to be confirmed. The reconstruction quality and potentially the training speed may benefit from different binarisation strategies, such as the straight-through estimator [27], but more work and comparisons are needed. Similarly, different overall training strategies and different decoding networks might be beneficial, such as VAEs [28] and unrolled architectures [29]. Additionally, the standardisation of the latent space could be surpassed by making the decoder scale-invariant as explained in [30, 31], which could improve multispectral reconstructions.

Our findings pave the way for real-time multispectral fluorescence microscopy. Indeed, the short time (50 ms) needed for reconstruction is compatible with acquisitions at a frame rate greater than 10 fps. This enables fluid visualisation that could find applications in the intraoperative field. In conclusion, we have demonstrated that learned approaches are necessary for more efficient compression, faster reconstruction times, and improved reconstruction quality, thereby extending the applicability of single-pixel fluorescence microscopes to real-time scenarios.

Funding

The authors acknowledge financial support by the UK government’s Horizon Europe funding guarantee (grant number EP/X030733/1) and the European Union (GA 101072354). Views and opinions expressed are, however, those of the author(s) only and do not necessarily reflect those of the European Union, the UK government, or the European Research Executive Agency. Neither the European Union nor the granting authority can be held responsible for them.

References

- [1] Gregor PC Drummen. Fluorescent probes and fluorescence (microscopy) techniques—illuminating biological and biomedical research. *Molecules*, 17(12):14067–14090, 2012.
- [2] Yasushi Hiraoka, Takeshi Shimi, and Tokuko Haraguchi. Multispectral imaging fluorescence microscopy for living cells. *Cell structure and function*, 27(5):367–374, 2002.
- [3] Lanlan Zhou and Wafik S. El-Deiry. Multispectral fluorescence imaging. *Journal of Nuclear Medicine*, 50(10):1563–1566, 2009.
- [4] Marco F. Duarte, Mark A. Davenport, Dharmpal Takhar, Jason N. Laska, Ting Sun, Kevin F. Kelly, and Richard G. Baraniuk. Single-pixel imaging via compressive sampling. *IEEE Signal Processing Magazine*, 25(2):83–91, March 2008.
- [5] Alberto Ghezzi, Armin J. M. Lenz, Fernando Soldevila, Enrique Tajahuerce, Vito Vurro, Andrea Bassi, Gianluca Valentini, Andrea Farina, and Cosimo D’Andrea. Computational based time-resolved multispectral fluorescence microscopy. *APL Photonics*, 8(4):046110, April 2023.
- [6] D.L. Donoho. Compressed sensing. *IEEE Transactions on Information Theory*, 52(4):1289–1306, April 2006.
- [7] Catherine F. Higham, Roderick Murray-Smith, Miles J. Padgett, and Matthew P. Edgar. Deep learning for real-time single-pixel video. *Scientific Reports*, 8(1):2369, February 2018.
- [8] Youquan Deng, Rongbin She, Wenquan Liu, Yuanfu Lu, and Guangyuan Li. Single-pixel imaging based on deep learning enhanced singular value decomposition. *Sensors*, 24(10):2963, January 2024.
- [9] Haiyan Liu, Xuyang Chang, Jun Yan, Pengyu Guo, Dong Xu, and Liheng Bian. Masked autoencoder for highly compressed single-pixel imaging. *Optics Letters*, 48(16):4392, August 2023.
- [10] Graham M. Gibson, Steven D. Johnson, and Miles J. Padgett. Single-pixel imaging 12 years on: a review. *Optics Express*, 28(19):28190, September 2020.
- [11] Richard G. Baraniuk. Compressive sensing [lecture notes]. *IEEE Signal Processing Magazine*, 24(4):118–121, July 2007.
- [12] Nam Huynh, Edward Zhang, Marta Betcke, Simon Arridge, Paul Beard, and Ben Cox. Single-pixel optical camera for video rate ultrasonic imaging. *Optica*, 3(1):26–29, Jan 2016.
- [13] Leonid I. Rudin, Stanley Osher, and Emad Fatemi. Nonlinear total variation based noise removal algorithms. *Physica D: Nonlinear Phenomena*, 60(1–4):259–268, November 1992.
- [14] Chengbo Li, Wotao Yin, Hong Jiang, and Yin Zhang. An efficient augmented lagrangian method with applications to total variation minimization. *Computational Optimization and Applications*, 56(3):507–530, December 2013.
- [15] Hang Zhao, Orazio Gallo, Iuri Frosio, and Jan Kautz. Loss functions for image restoration with neural networks. *IEEE Transactions on Computational Imaging*, 3(1):47–57, March 2017.
- [16] Dmitry Ulyanov, Andrea Vedaldi, and Victor Lempitsky. Instance normalization: The missing ingredient for fast stylization. 2016.
- [17] Olaf Ronneberger, Philipp Fischer, and Thomas Brox. *U-Net: Convolutional Networks for Biomedical Image Segmentation*, volume 9351, page 234–241. Springer International Publishing, Cham, 2015.
- [18] Diganta Misra. Mish: A self regularized non-monotonic activation function. 2019.
- [19] Diederik P. Kingma and Jimmy Ba. Adam: A method for stochastic optimization. 2014.
- [20] Stanley Hua, Alex Lu, and Alan Moses. CytoImageNet, 2021.
- [21] Adam Coates, Andrew Ng, and Honglak Lee. An analysis of single-layer networks in unsupervised feature learning. In Geoffrey Gordon, David Dunson, and Miroslav Dudík, editors, *Proceedings of the Fourteenth International Conference on Artificial Intelligence and Statistics*, volume 15 of *Proceedings of Machine Learning Research*, pages 215–223, Fort Lauderdale, FL, USA, 11–13 Apr 2011. PMLR.
- [22] T Smith and J Guild. The C.I.E. colorimetric standards and their use. *Transactions of the Optical Society*, 33(3):73–134, January 1931.
- [23] Wolfgang Becker, Axel Bergmann, and Christoph Biskup. Multispectral fluorescence lifetime imaging by tcspc. *Microscopy research and technique*, 70(5):403–409, 2007.
- [24] Tim Sanchez, Tianren Wang, Marta Venturas Pedro, Man Zhang, Ecem Esencan, Denny Sakkas, Dan Needleman, and Emre Seli. Metabolic imaging with the use of fluorescence lifetime imaging microscopy (flim) accurately detects mitochondrial dysfunction in mouse oocytes. *Fertility and Sterility*, 110(7):1387–1397, December 2018.

- [25] Kavon Karrobi, Anup Tank, Mohammad Ahsan Fuzail, Madhumathi Kalidoss, Karissa Tilbury, Muhammad Zaman, Jacopo Ferruzzi, and Darren Roblyer. Fluorescence lifetime imaging microscopy (flim) reveals spatial-metabolic changes in 3d breast cancer spheroids. *Scientific Reports*, 13(1):3624, March 2023.
- [26] F. Soldevila, A. J. M. Lenz, A. Ghezzi, A. Farina, C. D’Andrea, and E. Tajahuerce. Giga-voxel multidimensional fluorescence imaging combining single-pixel detection and data fusion. *Optics Letters*, 46(17):4312, September 2021.
- [27] Yoshua Bengio, Nicholas Léonard, and Aaron Courville. Estimating or propagating gradients through stochastic neurons for conditional computation. *arXiv preprint arXiv:1308.3432*, 2013.
- [28] Diederik P Kingma and Max Welling. Auto-encoding variational bayes. 2013.
- [29] Shanshan Wu, Alexandros G. Dimakis, Sujay Sanghavi, Felix X. Yu, Daniel Holtmann-Rice, Dmitry Storcheus, Afshin Rostamizadeh, and Sanjiv Kumar. Learning a compressed sensing measurement matrix via gradient unrolling. 2018.
- [30] Kai Zhang, Yawei Li, Wangmeng Zuo, Lei Zhang, Luc Van Gool, and Radu Timofte. Plug-and-play image restoration with deep denoiser prior. 2020.
- [31] Sreyas Mohan, Zahra Kadkhodaie, Eero P. Simoncelli, and Carlos Fernandez-Granda. Robust and interpretable blind image denoising via bias-free convolutional neural networks. 2019.